Journal of Alloys and Compounds 860 (2020) 158501

Contents lists available at ScienceDirect

Journal of Alloys and Compounds

journal homepage: www.elsevier.com/locate/jalcom

Scalable synthesis of highly luminescent and stable thiocyanate based $CsPbX_3$ perovskite nanocrystals for efficient white light-emitting diodes

Saroj Thapa, Gopi Chandra Adhikari, Hongyang Zhu*, Peifen Zhu*

Department of Physics and Engineering Physics, The University of Tulsa, Tulsa, OK 74104, United States

ARTICLE INFO

Article history:
Received 10 November 2020
Received in revised form 22 December 2020
Accepted 23 December 2020
Available online 25 December 2020

Keywords:
Lead halide perovskites
SCN^--based nanocrystals
Moisture stability
3-D printed conversion layers
White light-emitting diodes

ABSTRACT

All-inorganic lead halide perovskites have attracted considerable attention as promising materials for optoelectronic devices because of their excellent photophysical properties. However, the stability issue of halide perovskites precludes their practical applications. For the first time, this work exhibits that the optical properties and stability of $CsPbX_3$ perovskite nanocrystals (NCs), prepared by the saponification precipitation method, can be improved using thiocyanate (SCN^-). Besides, this work offers a simple and economical synthesis method operable at room temperature and ambient atmosphere. Specifically, an increasing concentration of SCN^- induces an increase in quantum yield almost by 10% and stability against air and moisture over several days due to the better passivation of trap states, irrespective of size and shape variation of NCs. The demonstration of tunable emission (454–645 nm) across the visible spectrum and the design of 3-D printed thin layers facilitate the preparation of green, yellow, and red-emitting color conversion layers. Benefitted from the decreased photon loss in as-synthesized conversion layers, the application of these color conversion layers results in a bright neutral white light (5184 K) with remarkable optical properties. Hence, this experimental study offers a low-temperature synthetic path for the scalable preparation of high-quality $CsPbX_3$ NCs processed with SCN^- and reveals the practical applications of such NCs.

1. Introduction

All-inorganic lead halide perovskites ($CsPbX_3$) nanocrystals (NCs) offer outstanding optoelectronic properties including narrow linewidth emission, tunable bandgaps, tunable emission across the whole visible spectrum depending on the NCs size and halide ion composition, and high photoluminescence quantum yield (PLQY) [1–9]. As a result, the perovskite NCs are widely used in designing modern optoelectronic devices such as solar cells, light-emitting diodes (LEDs), photodetectors, and lasers [10–14]. Despite these potentials, the halide-based perovskites easily decompose in an ambient atmosphere in the presence of moisture, air, and light, owing to the low formation energy, highly ionic nature, and massive surface defects due to the large surface-to-volume ratio of NCs [15,16]. This intrinsic instability of inorganic perovskite NCs seriously impedes their large-scale commercial and industrial applications. Therefore, the development of effective approaches including synthesis techniques is still needed to boost the stability and application of this type of material in optoelectronic devices.

Tremendous efforts have been devoted to improving the stability of lead halide perovskites. The use of a polymeric matrix such as poly (methyl methacrylate), poly(maleic anhydride-alt-1-octadecene), polystyrene, and poly(butyl methacrylate), or inorganic layer of silica and alumina on the surface of the perovskite quantum dots are widely investigated [17–19]. The use of compact polymer or inorganics coating exhibits improved stability against moisture and air. However, the electric and the optical properties are degraded making them relatively less suitable for optoelectronic devices [20]. Recently, a few theoretical and experimental studies demonstrated that the introduction of SCN^- can lead to a stable perovskite crystal structure with enhanced air and moisture tolerance caused by the strong interaction between Pb^{2+} and SCN^-, improve crystalline quality and optical properties by controlling the nucleation-growth process and decreasing trap density [21–23]. Nevertheless, the prospects for low-temperature and large-scale fabrication route point out a promising research direction towards the future commercialization of SCN^--based perovskites. Motivated by these facts, for the first time, our research work aims to develop and explore the optoelectronic properties of SCN^--based $CsPbX_3$ NCs experimentally,

* Corresponding authors.
E-mail addresses: hongyang-zhu@utulsa.edu (H. Zhu), peifen-zhu@utulsa.edu (P. Zhu).

https://doi.org/10.1016/j.jallcom.2020.158501
0925-8388/

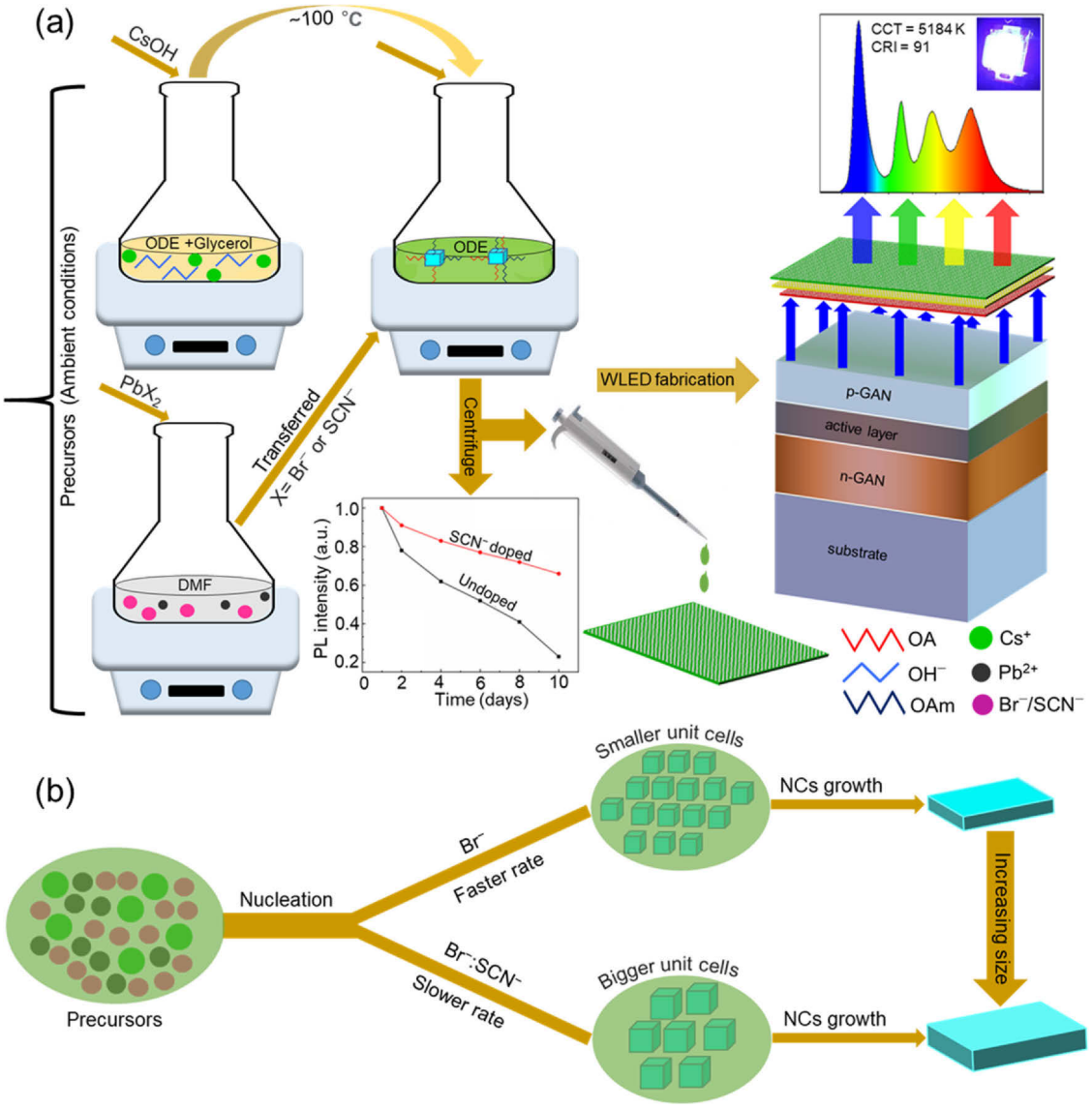

Fig. 1. Illustration of the (a) comprehensive strategy, starting from the material synthesis to the device fabrication for white light emission. Saponification precipitation method, operable at room temperature, allows us to synthesize the SCN^--based $CsPbX_3$ NCs that can be directly employed for preparing the 3-D printed different color conversion layers desirable for white light emission in combination with a blue LED and (b) schematics of the growth mechanism of the NCs. (For interpretation of the references to colour in this figure legend, the reader is referred to the web version of this article.)

employing the low-temperature synthesis approach, termed as the saponification precipitation (SP) method, and the comprehensive synthesis process is schematically shown in Fig. 1a [24]. This solution-processed synthesis technique is characterized by simple reaction setups, such as refraining from using inert environments, high reaction temperatures, and tedious preparation processes. Besides, the synthesis technique capable of synthesizing high-quality and relatively stable NCs has emerged as a legible, cost-effective, and time-saving synthesis approach and may be highly beneficial for the scale-up synthesis and commercialization of perovskite structures. The fact that the ease of synthesis and room temperature crystallization suits well for its applicability in low-cost optoelectronic devices with high efficiencies further stimulates us to fabricate the white light-emitting diodes (WLEDs) based on $CsPbX_3$ NCs processed with SCN^-, which has not been demonstrated experimentally until now.

In this work, we present a comprehensive study of the synthesis, properties, and functional applications of SCN^--based $CsPbX_3$ NCs ($X = Br^-$ or a mixture of Br^-/I^-). By adjusting the amount of $Pb(SCN)_2$ in the precursor solutions, compositionally diverse $CsPbX_3$ NCs were synthesized at room temperature and ambient atmosphere using the SP method whose optoelectronic properties were compared to the similar NCs synthesized using the much more complicated hot-injection (HI) method [1]. This simple and economical synthesis technique not only improves the crystallinity of the NCs (independent of the halide content) with increasing concentrations of SCN^- but also alters the lattice constant, confirming the effect of SCN^- in the $CsPbX_3$ matrix. Furthermore, the optoelectronic properties including the photoluminescence (PL) emission, full width at half maximum (FWHM) of PL emission, and the bandgap energy of as-prepared NCs depend on the concentration of SCN^-. Surprisingly, an increasing concentration of SCN^- results in decreasing emission linewidth due to the elimination of trap states which leads to an increase in PL quantum yield almost by 10%, and stability against air and moisture for more than 10 days. An increasing trend in the luminescent properties is independent of the size and shape variation of NCs. The tunable emissions across the significant portion of the visible spectrum (454–645 nm) with narrow FWHM (30–36 nm) are

obtained by engineering the composition of Br^-/I^- at 20% of SCN^- in $CsPbX_3$ NCs, which are beneficial to fabricating WLEDs. Hence, the use of 3-D printed thin color conversion layers for different color emitting (green, yellow, and red-emitting) NCs in WLED produces bright white light with a luminous efficacy of radiation (LER) of 301 lm/W, a general color-rendering index (CRI) of 91, and a correlated-color temperature (CCT) of 5184 K.

2. Materials and methods

2.1. Synthesis of SCN^--based $CsPbX_3$ NCs

2.1.1. Saponification precipitation method

An equimolar ratio of cesium hydroxide (CsOH, 0.2 g) and glyceryl trioleate (0.433 mL) was mixed in a beaker along with 3 mL of an octadecene (ODE) to obtain 0.4 M Cs-oleate precursor. The mixture was dried inside a vacuum oven for ~ 10 min at 120 °C. Similarly, to obtain the 0.4 M-precursor solution of $PbBr_2/PbI_2/Pb(SCN)_2$, the corresponding salt (0.735/0.922/0.674 g) was dissolved into dimethylformamide (DMF, 5 mL) separately. Preheated (~ 100 °C) Cs-oleate solution (0.05 mL) was mixed with a solution containing ODE (2.5 mL), oleylamine (OLA, 0.25 mL), and oleic acid (OA, 0.25 mL) with magnetic stirring. To obtain the colloidal suspension of $CsPbBr_3$ NCs, $PbBr_2$ precursor (0.4 mL) was swiftly injected into the above mixture followed by quick addition of acetone (10 mL) at room temperature. For obtaining the SCN^--based $CsPbBr_3$ NCs, the specific molar quantity of $Pb(SCN)_2$ and $PbBr_2$ in the precursor solution (loading to a total volume of 0.4 mL) were mixed in the desired ratio. The desired molar quantity of $Pb(SCN)_2$ expressed in percentage can be obtained by changing the molar ratio of $Pb(SCN)_2$ and $PbBr_2$. Finally, the colloidal solution was centrifuged for 10 min at 2000 rpm and subsequently washed with toluene to yield the desired $CsPbBr_3$ and SCN^--based $CsPbBr_3$ NCs, respectively. As-obtained NCs were redispersed into the toluene for further study. A similar process was repeated for the synthesis of SCN^--based mixed halide $CsPb(Br_{0.3}I_{0.7})_3$ NCs with the proportionate molar ratio of $PbBr_2/PbI_2/Pb(SCN)_2$ precursors. Furthermore, for obtaining the tunable emission across the visible spectrum, the composition of mixed halide (Br^-/I^-) was modulated in a proportionate molar ratio including 20% of SCN^-.

2.1.2. Hot-injection method

To prepare the Cs-oleate precursor, 0.163 g of cesium carbonate (Cs_2CO_3) was added into a 25 mL flask containing 0.5 mL of OA and 8 mL of ODE. The mixture was placed inside the vacuum oven allowing it to dry for ~ 1 h at 120 °C. The mixture was then heated under N_2 to 150 °C until Cs_2CO_3 completely reacts with OA resulting in a clear solution. For the preparation of lead salt precursors, 0.188 mmol of $PbBr_2$ (0.069 g) and $Pb(SCN)_2$ (0.061 g) were separately placed into a 25 mL flask containing a mixture of ODE (5 mL), OA (0.5 mL), and OLA (0.5 mL) that were dried in a vacuum oven at 120 °C for 1 h. Furthermore, these mixtures were placed on the top of a hot plate and allowed to stir at ~ 90 °C using the magnetic stirrer until the lead salts were completely dissolved. Cs-oleate solution (0.4 mL, preheated to 100 °C before injection) was quickly injected into the solution obtained by mixing the proportionate amount of $PbBr_2$ and $Pb(SCN)_2$ precursors maintained at 150 °C. The amount of $PbBr_2$ and $Pb(SCN)_2$ is tuned in a similar way as described in the SP synthesis approach. The resulting solution was placed into the ice-water bath where it was allowed to cool (for ~ 3 min). The as-obtained solution of the NCs was centrifuged at 3500 rpm for 10 min. The precipitated NCs were separated from the supernatant. Finally, the as-obtained precipitate of NCs was mixed with toluene for storage and characterization.

2.2. Device fabrication

For the fabrication of the device, we adopted a similar technique discussed in our previous work and schematically shown in Fig. 1a [25]. In brief, firstly, the 3-D printed substrates were coated with three different colors (green, yellow, and red)-emitting NCs separately. For this, a small amount of perovskite colloidal suspension (in toluene) was dropped across the substrate. The small channel hole available in the substrate allowed the NCs to spread throughout the surface due to capillary action. This was followed by the drying of the conversion layer components in an ambient atmosphere without encapsulation. Moreover, a thin layer of oil was used to coat the conversion layer to provide an encapsulation from environmental elements, and moisture. Finally, as-prepared conversion layers were stacked on top of a blue LED chip with an emission peak wavelength ~ 450 nm that runs at 6.05 mA and 5.5 V.

2.3. Characterization

To obtain the X-ray Diffractometer (XRD) patterns of as-prepared NCs, we employed a Rigaku SmartLab diffractometer with CuKα1 radiation (λ = 1.54 Å) operated at 40 kV and 44 mA. The transmission electron microscope (TEM) images obtained using the Hitachi H-7000 transmission microscope operated at 75 kV were used to study the morphological properties of the samples. The PL spectra and the UV–visible spectra were recorded by utilizing a spectrofluorophotometer (Shimadzu, RF6000) and a Varian Carry 50 Scan UV spectrophotometer, respectively. The absolute PLQYs were measured using a QE-pro spectrometer (QEP02037, Ocean Optics) coupled with an integrating sphere (819C-SF-6, Newport) excited by a laser source at a wavelength of 405 nm. PLQYs were estimated from averages of 3 different measurements. QE-pro spectrometer (QEP02037, Ocean Optics) in combination with Keithley 2450 source unit and LED chip (λ = 450 nm, operated at 6.05 mA and 5.5 V under forward bias) was used to record the Electroluminescence (EL) spectra. The optical properties of white light, including CCT, CRI, Commission Internationale de l'Eclairage (CIE) coordinates, and LER were estimated following the method shown in our previous work [26]. The CCT of a light source is a metric that characterizes the appearance of the emitted light. The CRI describes the ability of a light source to accurately reproduce the colors of the object it illuminates. All the measurements were performed at room temperature.

3. Results and discussion

3.1. SCN^--based $CsPbBr_3$ NCs

Here, the crystal structure, morphology, and optical properties of $CsPbBr_3$ perovskite NCs synthesized (using SP technique) with the addition of different molar concentrations of $Pb(SCN)_2$ have been investigated. The molar concentration of $Pb(SCN)_2$ is varied from 0% to 15% with respect to $PbBr_2$. The XRD patterns (Fig. 2a) are used to study the crystalline behavior of the NCs. The main diffraction peaks are located at ~15°, 21°, 30°, and 38° which belongs to (100), (110), (200), and (211) planes of cubic structure, respectively. However, the observed crystalline phase can be considered as pseudo-cubic rather than the pure cubic phase because the $CsPbBr_3$ NCs feature an orthorhombic phase at the unit cell level [27]. Although the crystal growth is not structurally affected by the addition of $Pb(SCN)_2$, we, however, observed a slight shift of the diffraction peak towards a lower 2θ range with increasing content of SCN^- which is due to the introduction of larger SCN^- (2.17 Å) in comparison to the smaller Br^- (1.96 Å) [28]. The shift in peak position by ~ 0.641° indicates the expansion of the lattice where the lattice constant increases from 5.861 Å to 5.963 Å. The splitting of the peak shape of the (200) plane

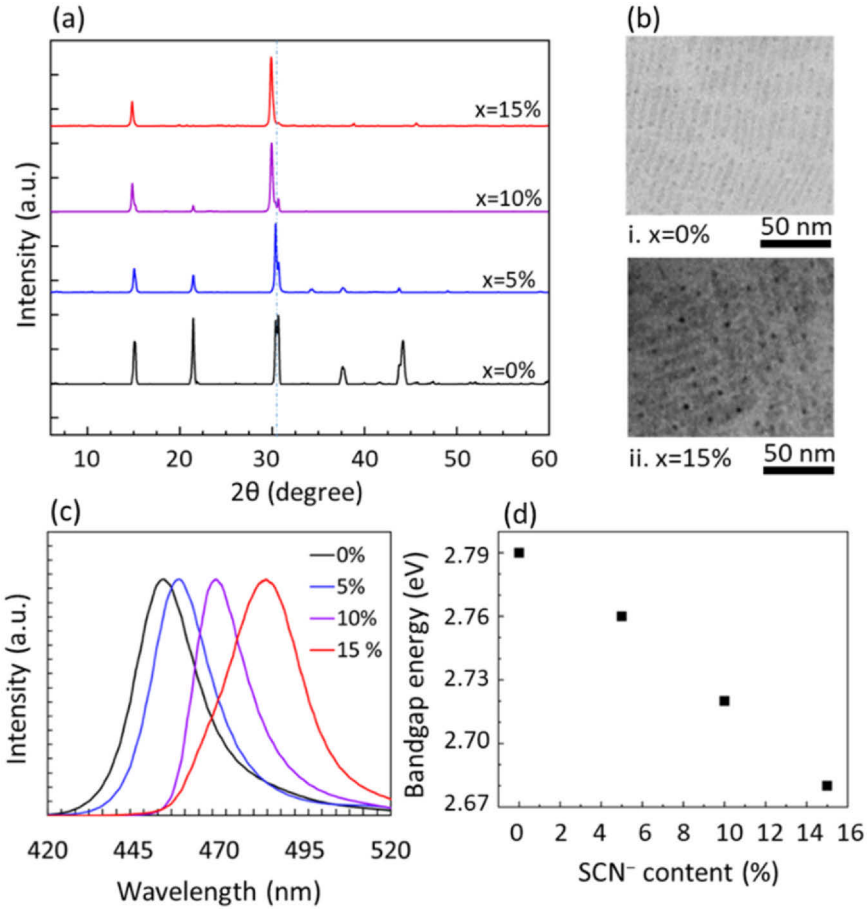

Fig. 2. (a) XRD patterns, (b) TEM images, (c) PL emission spectra, and (d) the variation of bandgap energy as a function of SCN^- content of SCN^--based $CsPbBr_3$ NCs synthesized using the SP method at a different molar concentration of SCN^-.

for the $CsPbBr_3$ host NCs gradually reduces with the increasing content of SCN^-, which shows the improvement in the crystallinity of NCs. The enhanced crystallization is due to the introduction of SCN^- which offers stronger bonding interactions between Pb^{2+} and SCN^- compared to that in-between Pb^{2+} and Br^- [21]. Moreover, the FWHM of the diffraction peaks corresponding to the (200) plane decreases from 0.447° (for 0% of SCN^-) to 0.291° (for15% of SCN^-). Lower FWHM values suggested a narrowing of the peaks that results from the higher degree of crystallization in the perovskite structures. Besides, the reduction in FWHM corresponds to the increasing dimensions of the NCs (discussed in the latter part) according to the Debye–Scherrer equation, $D = K\lambda/(\beta\cos\theta)$, where D is the average crystal size, K is the Scherrer constant, λ is the X-ray wavelength, β is the FWHM of the diffraction peak, and θ is the diffraction angle. The narrower diffraction peak and the stronger intensity corresponding to the (200) plane indicate the anisotropic growth of the resulting products. The clear and sharp XRD peaks without any intermediate phase demonstrate the successful incorporation of SCN^- into the host NCs and the presence of a uniform strain throughout the lattice of the material [23].

The TEM images were taken to study the morphology of as-prepared NCs. The shape and orientation NCs are documented as nanoplatelets (Figs. 2b and S1), similar to the previous report on the low-temperature synthesis of $CsPbBr_3$ NCs [2,29]. The implications of a synthesis temperature regulate the morphology of the growing NCs and the injection of acetone in a mixture of chemical precursors promote the nucleation and growth of NCs [2,30]. The TEM images indicate that the shapes of the resulting NCs are constructed in the form of nanoplatelets. The shape of the NCs remains unaltered even after the introduction of SCN^-, except for a slight variation in the dimensions. The average thickness of the nanoplatelets changes from ~ 2.89 nm (for x = 0%) to ~ 3.79 nm (for x = 15%) which is between 4 and 7 unit cells thick and the lateral size increases from ~ 19.07 nm (for 0% of SCN^-) to ~ 28.17 nm (for 15% SCN^-). The growth mechanism of the NCs depends on the nucleation and growth rates of the associated crystals. When the rate of nucleation is greater than the growth rate, we expect the growing NCs to be of smaller size and vice versa. The higher nucleation rate results in the generation of numerous nuclei that promotes the growth of smaller-sized NCs whereas the slower nucleation rate leads to the development of less number of nuclei that advances the formation of NCs of larger dimensions. This rate of nucleation further depends on the Gibbs free energy of the materials [31]. In our study, the introduction of SCN^- during the synthesis of SCN^-based $CsPbBr_3$ NCs is expected to increase the Gibbs free energy for nucleation compared to the $CsPbBr_3$ host NCs due to the chemical heterogeneity effect of SCN^- [22]. This increase in Gibbs free energy for nucleation retards the nucleation rate yielding the NCs of increasing size compared to the host NCs, which is schematically shown in Fig. 1b. The small changes in the dimensions of the NCs result in the spectral shifts which will be discussed in the latter part. It should be noted that the platelets being extremely sensitive to the electron beam tend to degrade and lose their crystallinity upon imaging the NCs with an electron beam. Thus, the observed spherical black dots in TEM images correspond to metallic Pb^{2+} nanoparticles suggesting that the part of the Pb^{2+} is reduced to metallic Pb^{2+} during acquisition [2,32].

The optical properties of as-grown NCs are investigated by measuring PL emission spectra (Fig. 2c) and absorption spectra

Table 1
PL emission peak, FWHM, bandgap, and PLQY of SCN^--based $CsPbBr_3$ NCs synthesized using the SP method at a different molar concentration of SCN^-.

SCN^- content (%)	PL peak (nm)	FWHM (nm)	Bandgap (eV)	PLQY (%)
0	454	21	2.79	70
5	459	20	2.76	77
10	469	18	2.72	80
15	484	26	2.68	78

(Fig. S2a). The PL emission peak is red-shifted from 454 nm to 484 nm with increasing SCN^- concentrations, under an excitation light of 365 nm. This shift can be attributed to the increasing thickness of the nanoplatelets (which is in between to 4–7 unit cells thick) because the thickness of the nanoplatelets is always a multiple of a single perovskite layer that leads to discrete energy levels [33]. Besides, this might be further attributed to the formation of new states just below the conduction band upon SCN^- introduction, which enhanced the interaction between the SCN^- and decreased the energy of related emission [34]. The narrower FWHM of PL emission (21–26 nm, Table 1) for the different concentrations of SCN^- confirms the high color purity of light emission. The FWHM decreases subsequently with an increase in the content of SCN^- (up to 10%) and increases when the content of SCN^- is increased to 15%. This regime further implies that the introduction of SCN^- decreases the defect density in the structure until a critical doping concentration, after which, doping promotes defect complexes in the structure [35]. This accounts for the unusual variation in the optical properties of as-grown NCs after a critical doping concentration. The shift in the UV–visible absorption peak is similar to the shift in the PL emission peak. The $CsPbBr_3$ NCs has an absorbance peak at around 443 nm, which is red-shifted to 464 nm when doped with 15% of SCN^-. The absorbance spectra for all the samples show a well-defined absorption peak (Fig. S2a), which resembles the larger exciton binding energy of the NCs. Besides, the sharper excitonic absorption feature implies a narrower size distribution of particles which is in agreement with TEM images. The observed change in the PL emission and the UV–visible peaks is consistent with the previous studies on the SCN^--based hybrid halide perovskite NCs that were obtained using the low-temperature synthesis approach [28,36]. The corresponding absorption peak is used for estimating the bandgap energy of perovskite NCs. The bandgap energy decreases from 2.79 eV to 2.68 eV with an increase in the content of SCN^- which is shown in Fig. 2d and summarized in Table 1. The nanoplatelets with the thickness equal to or greater than 3 unit cells thick likely to be in the weak confinement regime are expected to decrease the bandgap energy of nanoplatelets structures with increasing thickness [37]. Moreover, the decrease in bandgap energy can be confirmed through analysis of the relative energies of the halide and pseudohalide p orbitals. In SCN^-, the chalcogen p states are higher in energy than the Br^- p states such that they dominate the valence band maximum, resulting in reduced bandgap energy of the SCN^--based perovskite NCs [38,39]. The SCN^--based NCs show a Stokes shift of 9 nm between the absorption peak and PL peak, whereas that of $CsPbBr_3$ host NCs is 12 nm. The decrease in the Stokes shift of pseudohalide/halide mixed perovskite reveals a decrease in the non-radiative loss within the NCs, which makes them a promising candidate for optoelectronic applications. The NCs exhibit a high PLQY (≥ 78%) as shown in Table 1. The PLQY is augmented from ~ 70–80% when the amount of SCN^- is increased from 0% to 10% but slightly decreased to ~ 78% when the content of SCN^- further increased to 15% (Fig. S2b). Subsequent addition of SCN^--ligand solution might have repaired defects (initially hindering radiative recombination), enhancing the overall PLQY of the resulting NCs [23]. Furthermore, normalized PL excitation spectra of as-synthesized NCs are shown in Fig. S2c. The excitation spectra are measured by monitoring the corresponding peak emission wavelength. These spectra are broadband and almost identical in shape. The extension of excitation spectra from UV to the visible region covers the range of emission by the III-nitride UV/blue LEDs. Therefore, these perovskites can be effectively excited by the different light sources at that wide range of wavelengths and can serve as an efficient photon down-conversion in conjunction with III-nitride UV/blue LEDs to obtain white light.

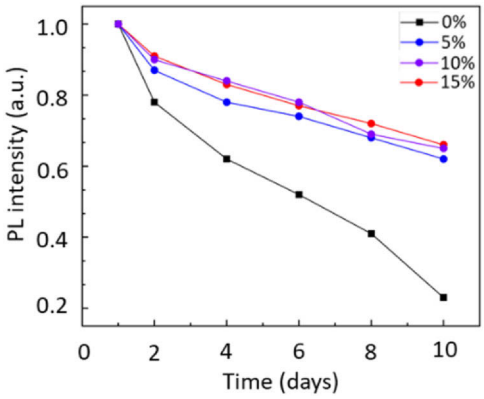

Fig. 3. Time-dependent variation of PL intensity of SCN^--based $CsPbBr_3$ NCs synthesized using the SP method at a different molar concentration of SCN^-.

Moreover, the air and moisture stability is analyzed by exposing the as-synthesized NCs in an ambient atmosphere for more than 10 days. The time-dependent PL intensity is shown in Fig. 3, which shows that the SCN^--based NCs retained as high as ~ 66% of their original intensity whereas the host NCs retained only ~ 21%. This demonstrates the stability of SCN^--based NCs compared to host NCs which is attributed to the stronger electrostatic interaction of SCN^- with Pb^{2+} that arises due to the larger formation energy between these two ions [21]. This improved stability would allow for these perovskites to be layered onto optoelectronic devices without an inert glovebox.

Further, to provide an insight into the effect of the synthesis approach, we synthesized a series of SCN^--based NCs at a different molar concentration of SCN^- (≤ 40%) using the HI method with a slight modification and present a comparative analysis of the two different experimental results. The effect observed in the structural, morphological, and optical properties of SCN^--based $CsPbBr_3$ NCs which were synthesized using the HI method is presented in Figs. 4, S3, and S4. In brief, the experimental results are consistent with the results obtained via the SP method. The measured XRD patterns (Fig. 4a) depict the cubic phase of as-synthesized NCs. The diffraction peak shift towards the lower angle by 0.121° (Fig. S3a) indicates the expansion of the lattice ranging from 5.82 Å (for 0% SCN^-) to 5.86 Å (for 40% of SCN^-). The FWHM of the corresponding diffraction peak decreases from 1.201° to 1.135°. The expansion of the lattice and the narrowing of the diffraction peaks indicate the formation of particles with increasing dimensions. The TEM images (Figs. 4b and S3b) of the as-synthesized NCs are independent of the concentration of SCN^- and are documented as cube-shaped NCs. The average size of the cube-shaped NCs estimated using the TEM images vary from ~ 7.64 nm to ~ 8.81 nm. Because the temperature plays a critical role in determining the shape and size of the resulting NCs, reactions conducted at 150 °C produce mostly symmetrical nanocubes with green-color PL emission [1]. The emission profile of as-grown NCs exhibit green emission (Fig. 4c) with the red-shifted emission peak (503–515 nm) and a narrow FWHM (21–28 nm) with the increasing content of SCN^-, as shown in Table 2. The use of UV–vis absorption spectra (Fig. S4a) for estimating the bandgap energy shows the decrease in its value from 2.41 eV (for 0% of SCN^-) to 2.34 eV (for 40% of SCN^-) which can be ascribed to the modification of halide and pseudohalide p orbitals with the introduction of SCN^- (Fig. 4d and

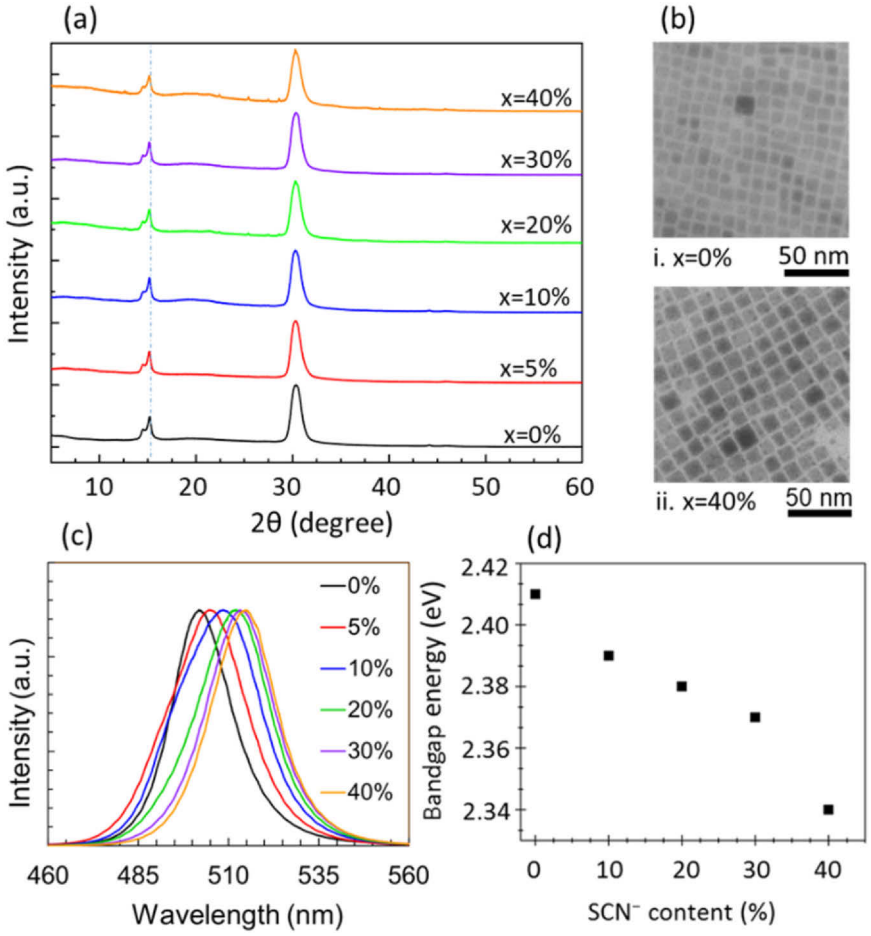

Fig. 4. (a) XRD patterns, (b) TEM images, (c) PL emission spectra, and (d) the variation of bandgap energy as a function of SCN^- content of SCN^--based $CsPbBr_3$ NCs synthesized using the HI method at a different molar concentration of SCN^-.

Table 2
PL emission peak, FWHM, bandgap, and PLQY of SCN^--based $CsPbBr_3$ NCs synthesized using the HI method at a different molar concentration of SCN^-.

SCN^- content (%)	PL peak (nm)	FWHM (nm)	Bandgap (eV)	PLQY (%)
0	503	22	2.41	76
5	507	25	2.40	79
10	509	28	2.39	83
20	512	23	2.38	87
30	513	22	2.37	89
40	515	21	2.34	86

Table 2). The PLQY of the as-prepared NCs increases from 76% to 89% (Table 2 and Fig. S4c). Moreover, the measured excitation spectra at a corresponding peak emission wavelength demonstrate the identical broadband spectra (260–480 nm) for the varying concentration of SCN^- (Fig. S4c).

3.2. SCN^--based mixed halide $CsPb(Br_{0.3}I_{0.7})_3$ NCs

The effect of SCN^- on the mixed halide perovskites $CsPb(Br_{0.3}I_{0.7})_3$ was investigated using structural, morphological, and optical properties which are shown in Figs. 5, S5, and S6. The NCs were synthesized using the SP method at room temperature for a different molar concentration of SCN^- (0–60%). The XRD patterns of $CsPb(Br_{0.3}I_{0.7})_3$ with various amounts of SCN^- are shown in Fig. 5a. These patterns demonstrate that the main diffraction peaks at ~ 20°, 27°, and 38° corresponding to (110), (111), and (211) planes of cubic structure, respectively. However, with an increase in the content of SCN^-, we noticed a diffraction peak shift towards a lower 2θ range demonstrating the effect of SCN^- into the perovskite lattice host. The diffraction peak shift by 0.168° confirms the expansion of the lattice constant within the unit cell that increases from 6.607 Å to 6.648 Å. This experimental observation is in line with the results reported in the previous literature [23,40]. The estimated diffraction peak width of 0.862°, 0.835°, 0.736°, and 0.714° corresponding to 0%, 20%, 40%, and 50% of SCN^- suggested the narrowing of the peaks due to the improvement in the crystallinity of the NCs. The lower angle diffraction peak at $2\theta \approx 6°$ in the XRD patterns demonstrates the intercalation of DMF into the PbI_2 interlayer space. As PbI_2 crystal has a layered structure, DMF can intercalate into the PbI_2 interlayer space and screen PbI_2 via Pb-O bonding [41,42]. The corresponding TEM images of as-grown NCs are shown in Figs. 5b and S5. The NCs possess a non-cubic morphology with different dimensions for different concentrations of SCN^-. A similar morphology on halides mixed (Br^-/I^-) NCs was reported in the previous study [43]. The mean length of the NCs changes with the change in the molar content of SCN^- ranging from ~ 12.68 nm (for 0% SCN^-) to ~ 15.02 nm (for 60% SCN^-) indicating seeded growth. This size variation of the NCs is in agreement with the change in the lattice constant of the NCs.

The as-grown NCs further exhibit SCN^--dependent PL properties. With an increasing amount of SCN^-, the normalized PL emission spectra (Fig. 5c), excited under 425 nm, exhibits the blue-shifted emission peak (645–605 nm), decreasing narrower FWHM (37–31 nm), and high PLQY (> 80%), depicted in Table 3. As the calculated particle sizes of as-grown NCs are much larger than the effective Bohr radius, it is confirmed that the optical blue-shift in the PL emission might be due to the introduction of SCN^- instead of the

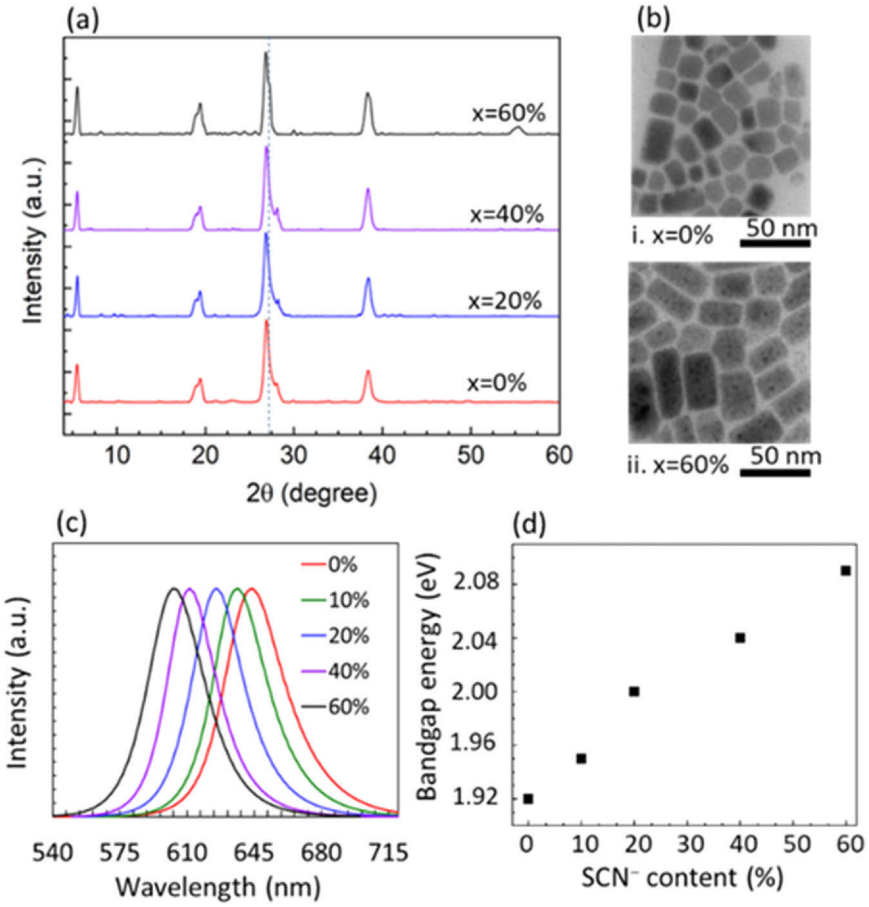

Fig. 5. (a) XRD patterns, (b) TEM images, (c) PL emission spectra, and (d) variation of bandgap energy as a function of SCN^- content of SCN^--based mixed halide $CsPb(Br_{0.3}I_{0.7})_3$ NCs synthesized using the SP method at a different molar concentration of SCN^-.

Table 3
PL emission peak, FWHM, bandgap, and PLQY of SCN^--based mixed halide $CsPb(Br_{0.3}I_{0.7})_3$ NCs synthesized using the SP method at a different molar concentration of SCN^-.

SCN^- content (%)	PL peak (nm)	FWHM (nm)	Bandgap (eV)	PLQY (%)
0	645	37	1.92	84
10	638	34	1.95	87
20	627	32	2.00	88
40	612	31	2.04	89
60	605	35	2.09	86

quantum confinement effect [1]. The introduction of SCN^- might have resulted in the existence of multiple transitions buried underneath the broad emission envelopes suggesting the spectral shift in the emission profile [23]. The reduced PL emission line-width accompanied by the blue-shifted emission peak indicates an improved quality of NCs with decrease intraband traps which reduce the dominant charge recombination phenomenon within the crystal structure [44]. This suggests the enhancement in the PLQY of the resulting NCs from ~ 84–89% (Fig. S6a and Table 3).

A linear profile of the absorption spectra is obtained (Fig. S6b), which indicates the formation of larger NCs. Owing to this, the bandgap was calculated using the Tauc plot (inset Fig. S6b) which increases from 1.86 eV to 2.09 eV (Fig. 5d). The substantial increase in the bandgap arises due to the effect of SCN^- into the perovskite matrix thereby reducing the Pb-I-P bond angles in three-dimensional perovskite structures [45]. A Stokes shift between the absorption and PL peaks, herein, also decreases from 24 nm to 12 nm when the content of SCN^- is increased from 0% to 60%. Furthermore, the normalized PL excitation spectra monitored at the corresponding emission peak are presented in Fig. S6c. These spectra are almost identical and broadband which spread over the wide wavelength region (280–580 nm). Additionally, the introduction of SCN^- is beneficial for improving the stability of the NCs and is indicated by the time-dependent PL intensity (Fig. 6). Fig. 6 shows that the SCN^--based NCs retained above ~ 65% of their original intensity whereas the host NCs retained only ~ 17% when exposed to air for more than 10 days in an ambient atmosphere. This confirms that the SCN^--based NCs hold superior luminescent properties compared to the host NCs. All these attributes suggest that the as-prepared NCs are a promising alternative to rare-earth elements contained traditional phosphors for fabricating the stable and energy-efficient WLEDs.

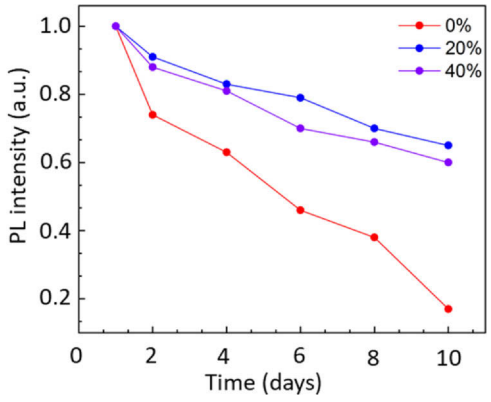

Fig. 6. Time-dependent variation of PL intensity of SCN^--based mixed halide $CsPb(Br_{0.3}I_{0.7})_3$ NCs synthesized using the SP method at a different molar concentration of SCN^-.

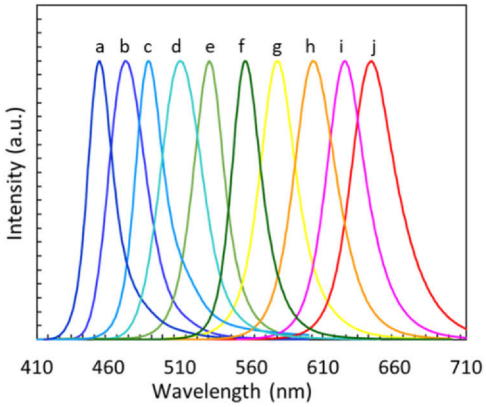

Fig. 7. Tunable PL emission spectra of mixed halide NCs for the different compositional modulation of Br^-/I^- with 20% of SCN^-.

Meanwhile, the PL properties of the as-synthesized products can be designed to cover the whole spectrum of visible light by tuning the composition of halides [46–48]. Herein, we synthesized a series of mixed halide and pseudohalide $CsPbX_3$ NCs by modulating the composition of (Br^-/I^-) anions at 20% of SCN^-. The XRD patterns of as-synthesized NCs (Fig. S7) illustrate the cubic phase of the perovskite similar to that of the host NCs with a slight shift in the diffraction peak towards the lower angle with a proportionate decrease in Br^-/I^- ratio. The shift in the diffraction peak shows the variation of the lattice constant. The TEM images (Fig. S8) retained the identical morphology for different proportions of halides, however, the particle size is varied. With a decreasing Br^-/I^- ratio, the PL spectra (Fig. 7) show a continuous red-shift in their PL peak position (454–645 nm), broadening of emission line-widths (21–37 nm), and a blue-shift in the bandgap energy (2.79–1.88 eV) which is summarized in Table 4. The narrower line-width emission is considered to be saturated, placing the fluorescence color coordinates more towards the edge of the CIE chromaticity space which results in high color purity LEDs. Hence, we infer that the optical properties of as-prepared NCs are remarkable for designing the lighting devices, especially the LEDs.

3.3. Fabrication of WLED

Associated with the tunable PL emission that covers the whole visible wavelength range, narrow FWHM, and high PLQY, the SCN^--based $CsPbX_3$ perovskite NCs have huge potential to be used as color conversion layers in WLEDs for generating white light with high color quality. Hence, a prototype down-conversion WLED with a neutral white light is fabricated using the 3-D printed thin layers containing SCN^--based perovskite NCs (green, yellow, and red) in conjunction with a blue LED chip (λ_{peak} ~ 450 nm, operating at 6.05 mA and 5.5 V). The high ionic mobility of the halide ions in the perovskite NCs results in the mixing of corresponding ions that governs the optical properties of the mixed composites [49]. The ease of halide exchange between perovskite NCs of different compositions can be considered both as a boon and a curse for perovskite materials [50]. The design of an efficient device structure consisting of layers of metal halide perovskites of different compositions is still challenging due to the mixing of halide ions which leads to the decomposition of the NCs to other phases and deteriorates their optical performances [50,51]. To overcome this limitation, herein, we adopted the use of a 3-D printed thin structure that can be used as a color conversion layer in fabricating the WLED. The preparation of a 3-D printed thin substrate and the corresponding color conversion layer is provided in detail in our previous publication [25]. Specifically, the 3-D printed thin substrates are uniquely designed with a rectilinear bottom infill because of which the colloidal suspension of color emitting NCs when drop cast on the top of the substrates will self-spread throughout the substrates via capillary action. Consequently, allowing the carrier fluid to evaporate completely, we obtain a thin coating of NCs with the NCs residing inside the printed substrate that finally serves as a color conversion layer. This attribute is highly preferred for creating an efficient LED structure with layers of metal halide perovskite NCs of different compositions intact. Thus, the superiority of the 3-D printed color conversion layers lies in the fact that they are capable of eliminating the undesirable mixing of different halide components while maintaining their fluorescence property. Herein, we prepared the different thin film of green (λ_{peak} ~ 532 nm), yellow (λ_{peak} ~ 578 nm), and red (λ_{peak} ~ 627 nm) emitting color conversion phosphors (contained with 20% of SCN^-) for the Br^-:I^- composition of 0.48:0.32, 0.40:0.40, and 0.30:0.50, respectively (Fig. 1a and Table 4). The different color emitting conversion layers are then stacked on the top of blue LED in a hierarchy of their increasing bandgap via a remote phosphor technique for generating the white light. The added benefit arises from the choice of PLA with a low refractive index (1.46) that impairs the photon loss from the source during the operation of the device structure. Additionally, the introduction of channels within the conversion layers, the elimination of machinery need for spin coating, and the coffee-ring effect likely to be observed on account of spin coating boosts the practical applicability of this approach in designing efficient optoelectronic devices, especially the LEDs.

Based on this device structure, we investigated the different optical behavior of the generated white light emission such as EL, CCT, CRI, CIE coordinates, D_{uv}, and LER. As shown in the inset of Fig. 8a, the WLED at a driving current of 6.05 mA generated saturated white emission with a high LER of 301 lm/W, a general CRI of 91, and CCT of 5148 K. These characteristics are superior to the previous report on WLEDs based on the polymer or metal-coated phosphors [52,53]. A CCT of 5184 K is the characteristic of a neutral white light. The corresponding EL spectrum (Fig. 8a) consists of four distinct emission peaks which belong to blue LED chip, green-, yellow-, and red-emitting NCs, respectively. The distinct peaks indicate the complete elimination of anion exchange reaction likely to be observed within these crystals. The EL spectrum further demonstrates that the blue and the green emissions have more contribution to obtaining this neutral white light in comparison to that of the yellow and the red emissions. The LER above 300 lm/W demonstrates the high vision performance of WLEDs and a light source with a general CRI in the 90s is excellent for indoor lighting [54]. Additionally, we estimated the special CRI (R_9-R_{15}) that are considered to be the most important figures of merit of white light source for the evaluation of color rendition. The R_9-R_{12} indicates the three saturated colors red, yellow, green, and blue whose value corresponds to 81, 93, 93, and 60, respectively. Increases in saturation yield better visual clarity and enhance perceived brightness. An R_9 score greater than 0 is generally considered acceptable. The R_9 is especially pertinent, as the

Table 4
PL emission peak, FWHM, and bandgap of mixed halides NCs for the different compositional modulation of Br^-/I^- with 20% of SCN^-.

ID	Halides content		PL peak (nm)	FWHM (nm)	Bandgap (eV)
	Br^-	I^-			
a	1	0	454	21	2.79
b	0.72	0.08	472	30	2.68
c	0.64	0.16	490	24	2.61
d	0.52	0.28	512	34	2.31
e	0.48	0.32	532	26	2.24
f	0.44	0.36	557	25	2.15
g	0.40	0.40	578	31	2.11
h	0.32	0.48	605	35	2.07
i	0.30	0.50	627	32	1.91
j	0.24	0.56	645	37	1.88

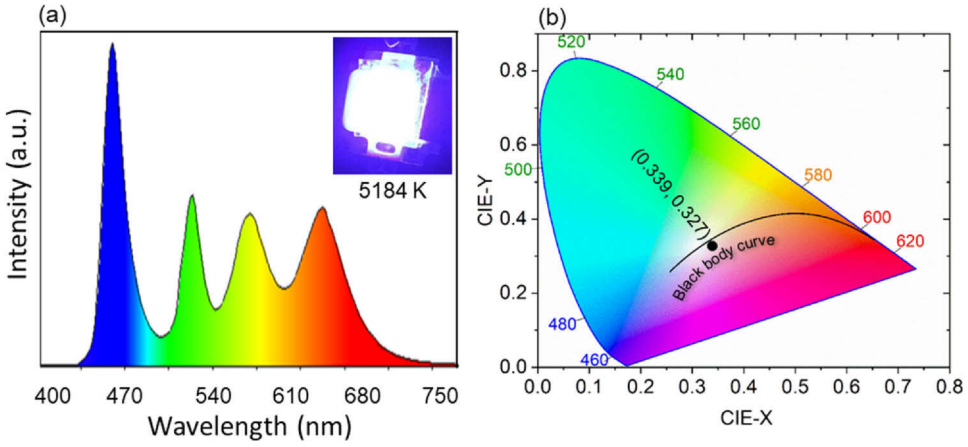

Fig. 8. (a) EL spectra of as-fabricated WLED (inset is the photograph of the same WLED) and (b) CIE coordinates of the corresponding white light emission. (For interpretation of the references to colour in this figure legend, the reader is referred to the web version of this article.)

rendition of saturated red is particularly important for the appearance of skin tones [55]. Moreover, the special CRIs (R_{13}, R_{14}, and R_{15}) corresponding to the Caucasian complexion (color of the skin on the face of European women), green leaf, and oriental complexion (color of the skin on the face of Chinese women) are also very high. Each of these values corresponds to 95, 99, and 89, respectively. Particularly, the high value of R_{13} and R_{15} are important for interior lighting [56]. Notably, these remarkable attributes are an indication of the fact that the as-fabricated WLED reproduces the color of an object precisely. This relatively high value of CRI and LER are due to the narrow line-width emission. The CIE coordinates (x, y) of neutral white light emission at a corresponding CCT are reflected on the CIE color coordinate diagram as shown in Fig. 8b. The CIE coordinates (0.339, 0.327) of this neutral white light almost overlaps with the Planckian with the recorded D_{uv} to be < 0.002. This concludes that the color temperature we obtained is comfortable for the human eyesight and has an energizing effect on the people. Furthermore, the CIE coordinates of the neutral white light (0.339, 0.327) is very close to the standard neutral white light (0.333, 0.333). Therefore, white light obtained using SCN^--based metal halide perovskites are promising materials to replace conventional phosphors in next-generation white LEDs that can be designed to be highly energy-efficient with high color purity.

4. Conclusion

In summary, a facile saponification precipitation synthesis method has been employed to synthesize high-quality SCN^--based $CsPbX_3$ NCs with controlled morphology and highly luminescent properties. The better passivation of the trap states and the stronger electrostatic interaction of SCN^- with Pb^{2+} provided due to the introduction of SCN^-, the increases in the PLQY, and the stability of resulting NCs. When stored in an ambient environment for several days, SCN^--based NCs maintain high PL intensity compared to the host NCs, suggesting the betterment in the stability of NCs against air and moisture. Through an appropriate compositional modulation of Br^-/I^- at 20% of SCN^-, a series of continuously tunable PL emission with narrow FWHM and high PLQY were obtained, which are desirable for white light emission. Thus, a photon down-converted WLED was fabricated in which the 3-D printed green-, yellow-, and red-emitting NCs were placed on top of the blue LED chip using the remote-phosphor architecture. This resulted in a bright neutral white light with a high LER of 301 lm/W, a general CRI of 91, CIE coordinates of (0.34, 0.33), D_{uv} < 0.002, and CCT of 5184 K. These remarkable features indicate the great potential of SCN^--based perovskite NCs to be used in WLEDs. In addition, these experimental findings indicate that the saponification precipitation method imparts remarkable luminescent properties comparable to that prepared by the HI method and, therefore, can be considered as a viable and economical synthesis method. For further research, we anticipate the use of the SP method to accelerate the discovery and rational design of state-of-the-art stable metal halide perovskites for various optoelectronic applications.

CRediT authorship contribution statement

Saroj Thapa: Investigation; Methodology, Data curation, Formal analysis, Writing - original draft, Writing - review & editing. **Gopi Adhikari**: Methodology, Formal analysis, Writing - review & editing. **Hongyang Zhu:** Conceptualization, Methodology Formal analysis, Writing - review & editing. **Peifen Zhu**: Conceptualization, Methodology, Formal analysis, Data interpretation, Writing - review & editing, Project administration and Supervision.

Declaration of competing interest

The authors declare that they have no known competing financial interests or personal relationships that could have appeared to influence the work reported in this paper.

Acknowledgments

This work is supported by the National Science Foundation (NSF) under Award No. 1945558. The authors would like to acknowledge Professor Parameswar Harikumar's help with absorption measurements and Professor Alexei Grigoriev's help with XRD measurements.

Appendix A. Supporting information

Supplementary data associated with this article can be found in the online version at 10.1016/j.jallcom.2020.158501.

References

[1] L. Protesescu, S. Yakunin, M.I. Bodnarchuk, F. Krieg, R. Caputo, C.H. Hendon, R.X. Yang, A. Walsh, M.V. Kovalenko, Nanocrystals of cesium lead halide perovskites ($CsPbX_3$, X = Cl, Br, and I): novel optoelectronic materials showing bright emission with wide color gamut, Nano Lett. 15 (2015) 3692–3696.
[2] Q.A. Akkerman, S.G. Motti, A.R. Srimath Kandada, E. Mosconi, V. D'Innocenzo, G. Bertoni, S. Marras, B.A. Kamino, L. Miranda, F. De Angelis, A. Petrozza, M. Prato, L. Manna, Solution synthesis approach to colloidal cesium lead halide perovskite nanoplatelets with monolayer- level thickness control, J. Am. Chem. Soc. 138 (2016) 1010–1016.

[3] Y. Wang, H. Sun, All-inorganic metal halide perovskite nanostructures: from photophysics to light-emitting applications, Small Methods 2 (2018) 1700252.
[4] L. Zhang, Q. Zeng, K. Wang, Pressure-induced structural and optical properties of inorganic halide perovskite $CsPbBr_3$, J. Phys. Chem. Lett. 8 (2017) 3752–3758.
[5] Y. Nagaoka, K. Hills-Kimball, R. Tan, R. Li, Z. Wang, O. Chen, Nanocube superlattices of cesium lead bromide perovskites and pressure-induced phase transformations at atomic and mesoscale levels, Adv. Mater. 29 (2017) 1606666.
[6] H. Zhu, T. Cai, M. Que, J.-P. Song, B.M. Rubenstein, Z. Wang, O. Chen, Pressure-induced phase transformation and band-gap engineering of formamidinium lead Iodide perovskite nanocrystals, J. Phys. Chem. Lett. 9 (2018) 4199–4205.
[7] Y. Zhang, J. Liu, Z. Wang, Y. Xue, Q. Ou, L. Polavarapu, J. Zheng, X. Qi, Q. Bao, Synthesis, properties, and optical applications of low-dimensional perovskites, Chem. Commun. 52 (2016) 13637–13655.
[8] L. Yang, Z. Li, C. Liu, X. Yao, H. Li, X. Liu, J. Liu, P. Zhu, B. Liu, T. Cui, C. Sun, Y. Bao, Temperature-dependent lasing of $CsPbI_3$ triangular pyramid, J. Phys. Chem. Lett. 10 (2019) 7056–7061.
[9] L. Wang, K. Wang, G. Xiao, Q. Zeng, B. Zou, Pressure-induced structural evolution and band gap shifts of organometal halide perovskite-based methylammonium lead chloride, J. Phys. Chem. Lett. 7 (2016) 5273–5279.
[10] A. Kojima, K. Teshima, Y. Shirai, T. Miyasaka, Organometal halide perovskites as visible-light sensitizers for photovoltaic cells, J. Am. Chem. Soc. 131 (2009) 6050–6051.
[11] K. Lin, J. Xing, L.N. Quan, F.P.G. de Arquer, X. Gong, J. Lu, L. Xie, W. Zhao, D. Zhang, C. Yan, W. Li, X. Liu, Y. Lu, J. Kirman, E.H. Sargent, Q. Xiong, Z. Wei, Perovskite light- emitting diodes with external quantum efficiency exceeding 20 per cent, Nature 562 (2018) 245–248.
[12] S. Thapa, G.C. Adhikari, H. Zhu, P. Zhu, Blue-red color-tunable all-inorganic bromide–iodide mixed-halide perovskite nanocrystals using the saponification technique for white-light- emitting diodes, J. Opt. Soc. Am. B 36 (2019) 1616–1622.
[13] P.L. Ramasamy, D.H. Kim, B. Lee, S.H. Lee, M.S. Lee, J.S. Lee, All-inorganic cesium lead halide perovskite nanocrystals for photodetector applications, Chem. Commun. 52 (2016) 2067–2070.
[14] Z. Li, J. Moon, A. Gharajeh, R. Haroldson, R. Hawkins, W. Hu, A. Zakhidov, Q. Gu, Room- temperature continuous-wave operation of organometal halide perovskite lasers, ACS Nano 12 (2018) 10968–10976.
[15] Q.A. Akkerman, G. Raino, M.V. Kovalenko, L. Manna, Genesis, challenges and opportunities for colloidal lead halide perovskite nanocrystals, Nat. Mater. 17 (2018) 394–405.
[16] Y. Wei, Z. Cheng, J. Lin, An overview on enhancing the stability of lead halide perovskite quantum dots and their applications in phosphor-converted LEDs, Chem. Soc. Rev. 48 (2019) 310–350.
[17] M. Meyns, M. Peralvarez, A. Heuer-Jungemann, W. Hertog, M. Ibanez, R. Nafria, A. Genc, J. Arbiol, M.V. Kovalenko, J. Carreras, A. Cabot, A.G. Kanaras, Polymer-enhanced stability of inorganic perovskite nanocrystals and their application in color conversion LEDs, ACS Appl. Mater. Interfaces 8 (2016) 19579–19586.
[18] Y. Xin, H. Zhao, J. Zhang, Highly stable and luminescent perovskite–polymer composites from a convenient and universal strategy, ACS Appl. Mater. Interfaces 10 (2018) 4971–4980.
[19] Z. Li, L. Kong, S. Huang, L. Li, Highly luminescent and ultrastable $CsPbBr_3$ perovskite quantum dots incorporated into a silica/alumina monolith, Angew. Chem. Int. Ed. 56 (2017) 8134–8138.
[20] L. Xi, C.B. Boothroyd, T. Salim, S. Borghardt, Y.M. Lam, B.E. Kardynał, Facile in situ synthesis of stable luminescent organic–inorganic lead halide perovskite nanoparticles in a polymer matrix, J. Mater. Chem. C 5 (2017) 7207–7214.
[21] Q.R. Jiang, D. Gong, J. Piacentino, E.L. Zheng, C. Xu, T. Pseudohalide-induced, moisture tolerance in perovskite $CH_3NH_3Pb(SCN)_2I$ thin films, Angew. Chem. Int. Ed. Engl. 54 (2015) 7617–7620.
[22] M.K. Kim, T. Jeon, H.I. Park, J.M. Lee, S.A. Nam, S.O. Kim, Effective control of crystal grain size in $CH_3NH_3PbI_3$ perovskite solar cells with a pseudohalide Pb $(SCN)_2$ additive, CrystEngComm 18 (2016) 6090–6095.
[23] A. Halder, R. Chulliyil, A.S. Subbiah, T. Khan, S. Chattoraj, A. Chowdhury, S.K. Sarkar, Pseudohalide (SCN^-)-doped $MAPbI_3$ perovskites: a few surprises, J. Phys. Chem. Lett. 6 (2015) 3483–3489.
[24] G.C. Adhikari, P.A. Vargas, H. Zhu, P. Zhu, Saponification precipitation method for $CsPbBr_3$ nanocrystals with blue-green tunable emission, J. Phys. Chem. C 123 (2018) 1406–1412.
[25] G.C. Adhikari, S. Thapa, H. Zhu, P. Zhu, Mg^{2+}-alloyed all-inorganic halide perovskites for white light-emitting diodes by 3D-printing method, Adv. Opt. Mater. 7 (2019) 1900916.
[26] P. Zhu, H. Zhu, G.C. Adhikari, S. Thapa, Design of circadian white light-emitting diodes with tunable color temperature and nearly perfect color rendition, OSA Contin. 2 (2019) 2413–2427.
[27] P. Cottingham, R.L. Brutchey, On the crystal structure of colloidally prepared $CsPbBr_3$ quantum dots, Chem. Commun. 52 (2016) 5246–5249.
[28] Y. Lou, Y. Niu, D. Yang, Q. Xu, Y. Hu, Y. Shen, J. Ming, J. Chen, L. Zhang, Y. Zhao, Rod- shaped thiocyanate-induced abnormal band gap broadening in SCN–doped $CsPbBr_3$ perovskite nanocrystals, Nano Res. 11 (2018) 2715–2723.
[29] B.J. Bohn, Y. Tong, M. Gramlich, M.L. Lai, M. Döblinger, K. Wang, R.L.Z. Hoye, P. Müller- Buschbaum, S.D. Stranks, A.S. Urban, L. Polavarapu, J. Feldmann, Boosting tunable blue luminescence of halide perovskite nanoplatelets through postsynthetic surface trap repair, Nano Lett. 18 (2018) 5231–5238.
[30] R.L.Z. Hoye, M.L. Lai, M. Anaya, Y. Tong, K. Galkowski, T. Doherty, W. Li, T.N. Huq, S. Mackowski, L. Polavarapu, J. Feldmann, J.L. MacManus-Driscoll, R.H. Friend, A.S. Urban, S.D. Stranks, Identifying and reducing interfacial losses to enhance color-pure electroluminescence in blue-emitting perovskite nanoplatelet light-emitting diodes, ACS Energy Lett. 4 (2019) 1181–1188.
[31] H. Taherianfard, G.-W. Kim, M.M. Byranvand, K. Choi, G. Kang, H. Choi, F. Tajabadi, N. Taghavinia, T. Park, Effective management of nucleation and crystallization processes in perovskite formation via facile control of antisolvent temperature, ACS Appl. Mater. Interfaces 3 (2020) 1506–1514.
[32] Z. Dang, J. Shamsi, F. Palazon, M. Imran, Q.A. Akkerman, S. Park, G. Bertoni, M. Prato, R. Brescia, L. Manna, In situ transmission electron microscopy study of electron beam-induced transformations in colloidal cesium lead halide perovskite nanocrystals, ACS Nano 11 (2017) 2124–2132.
[33] Y. Bekenstein, B.A. Koscher, S.W. Eaton, P. Yang, A.P. Alivisatos, Highly luminescent colloidal nanoplates of perovskite cesium lead halide and their oriented assemblies, J. Am. Chem. Soc. 137 (2015) 16008–16011.
[34] C. Yang, A. Faust, Y. Amit, I. Gdor, U. Banin, S. Ruhman, Impurity sub-band in heavily Cu- doped InAs nanocrystal quantum dots detected by ultrafast transient absorption, J. Phys. Chem. A 120 (2016) 3088–3097.
[35] G. Rainò, G. Nedelcu, L. Protesescu, M.I. Bodnarchuk, M.V. Kovalenko, R.F. Mahrt, T. Stöferle, Single cesium lead halide perovskite nanocrystals at low temperature: fast single- photon emission, reduced blinking, and exciton fine structure, ACS Nano 10 (2016) 2485–2490.
[36] T. Cai, F. Li, Y. Jiang, X. Liu, X. Xia, X. Wang, J. Peng, L. Wang, W.A. Daoud, In situ inclusion of thiocyanate for highly luminescent and stable $CH_3NH_3PbBr_3$ perovskite nanocrystals, Nanoscale 11 (2019) 1319–1325.
[37] J.A. Sichert, Y. Tong, N. Mutz, M. Vollmer, S. Fischer, K.Z. Milowska, R. Garcia Cortadella, B. Nickel, C. Cardenas-Daw, J.K. Stolarczyk, A.S. Urban, J. Feldmann, Quantum size effect in organometal halide perovskite nanoplatelets, Nano Lett. 15 (2015) 6521–6527.
[38] W.-J. Yin, J.-H. Yang, J. Kang, Y. Yan, S.-H. Wei, Halide perovskite materials for solar cells: a theoretical review, J. Mater. Chem. A 3 (2015) 8926–8942.
[39] A.M. Ganose, C.N. Savory, D.O. Scanlon, Electronic and defect properties of $(CH_3NH_3)_2Pb(SCN)_2I_2$ analogues for photovoltaic applications, J. Mater. Chem. A 5 (2017) 7845–7853.
[40] Q. Tai, P. You, H. Sang, Z. Liu, C. Hu, H.L.W. Chan, F. Yan, Efficient and stable perovskite solar cells prepared in ambient air irrespective of the humidity, Nat. Commun. 7 (2016) 11105.
[41] Y. Li, Z. Zhao, F. Lin, X. Cao, X. Cui, J. Wei, Real-time observation of iodide ion migration in methylammonium lead halide perovskites, Small 13 (2017) 1701711.
[42] F. Hao, C.C. Stoumpos, Z. Liu, R.P. Chang, M.G. Kanatzidis, Controllable perovskite crystallization at a gas-solid interface for hole conductor-free solar cells with steady power conversion efficiency over 10%, J. Am. Chem. Soc. 136 (2014) 16411–16419.
[43] G.C. Adhikari, P.A. Vargas, H. Zhu, A. Grigoriev, P. Zhu, Tetradic phosphor white light with variable CCT and superlative CRI through organolead halide perovskite nanocrystals, Nanoscale Adv. 1 (2019) 1791–1798.
[44] Y. Shao, Z. Xiao, C. Bi, Y. Yuan, J. Huang, Origin and elimination of photocurrent hysteresis by fullerene passivation in $CH_3NH_3PbI_3$ planar heterojunction solar cells, Nat. Commun. 5 (2014) 5784.
[45] M.R. Filip, G.E. Eperon, H.J. Snaith, F. Giustino, Steric engineering of metal-halide perovskites with tunable optical band gaps, Nat. Commun. 5 (2014) 5757.
[46] D.J. Freppon, L. Men, S.J. Burkhow, J.W. Petrich, J. Vela, E.A. Smith, Photophysical properties of wavelength-tunable methylammonium lead halide perovskite nanocrystals, J. Mater. Chem. C 5 (2017) 118–126.
[47] H. Chen, A. Guo, X. Gu, M. Feng, Highly luminescent $CsPbX_3$ (X"Cl, Br, I) perovskite nanocrystals with tunable photoluminescence properties, J. Alloy. Compd. 789 (2019) 392–399.
[48] Y. Tong, M. Fu, E. Bladt, H. Huang, A.F. Richter, K. Wang, P. MüllerBuschbaum, S. Bals, P. Tamarat, B. Lounis, J. Feldmann, L. Polavarapu, Chemical cutting of perovskite nanowires into single-photon emissive low-aspect-ratio $CsPbX_3$ (X= Cl, Br,I) nanorods, Angew. Chem. Int. Ed. 57 (2018) 16094–16098.
[49] Q.A. Akkerman, V. D'Innocenzo, S. Accornero, A. Scarpellini, A. Petrozza, M. Prato, L. Manna, Tuning the optical properties of cesium lead halide perovskite nanocrystals by anion exchange reactions, J. Am. Chem. Soc. 137 (2015) 10276–10281.
[50] M. Li, X. Zhang, S. Lu, P. Yang, Phase transformation, morphology control, and luminescence evolution of cesium lead halide nanocrystals in the anion exchange process, RSC Adv. 6 (2016) 103382–103389.
[51] Y. Su, Q. Jing, Y. Xu, X. Xing, Z. Lu, Preventing anion exchange between perovskite nanocrystals by confinement in porous SiO_2 nanobeads, ACS Omega 4 (2019) 22209–22213.
[52] H. Huang, B. Chen, Z. Wang, T.F. Hung, A.S. Susha, H. Zhong, A.L. Rogach, Water resistant $CsPbX_3$ nanocrystals coated with polyhedral oligomeric silsesquioxane and their use as solid state luminophores in all-perovskite white light-emitting devices, Chem. Sci. 7 (2016) 5699–5703.
[53] C. Sun, Y. Zhang, C. Ruan, C. Yin, X. Wang, Y. Wang, W.W. Yu, Efficient and stable white LEDs with silica-coated inorganic perovskite quantum dots, Adv. Mater. 28 (2016) 10088–10094.
[54] P. Zhu, H. Zhu, G.C. Adhikari, S. Thapa, Spectral optimization of white light from hybrid metal halide perovskites, OSA Contin. 2 (2019) 1880–1888.
[55] Solid-State Lighting Technology Fact Sheet-LED Color Characteristics, U.S. Department of Energy, 2016, https://www.energy.gov/sites/prod/files/2016/08/f33/led-color-characteristics-factsheet.pdf.
[56] W. Yang, P. Zhong, S. Mei, Q. Chen, W. Zhang, J. Zhu, R. Guo, G. He, Photometric optimization of color temperature tunable quantum dots converted white LEDs for excellent color rendition, IEEE Photonics J. 8 (2016) 1–11.